Research Article | Vol. 29, No. 3 / 1 February 2021 / Optics Express 4082
Optics EXPRESS

Imaging three-dimensional single-atom arrays all at once

HAEUN SUN,[1] YUNHEUNG SONG,[1,2] ANDREW BYUN,[1] HEEJEONG JEONG,[3] AND JAEWOOK AHN[1,*]

[1]*Department of Physics, KAIST, Daejeon 34141, Republic of Korea*
[2]*Currently with the Department of Physics, University of Wisconsin-Madison, 1150 University Avenue, Madison, Wisconsin 53706, USA*
[3]*Department of Physics, Faculty of Science, University of Malaya, Kuala Lumpur 50603, Malaysia*
[*]*jwahn@kaist.ac.kr*
http:qcl.kaist.ac.kr

Abstract: Simultaneous imaging of a three-dimensional distribution of point sources is presented. In a two-lens microscope, the point-spreads on the quasi-image plane, which is located between the Fourier and image planes, are spatially distinct, so a set of Fresnel lenslets can perform individual wave-front shaping for axial and lateral rearrangements of the images. In experiments performed with single atoms and holographically programmed lenslets, various three-dimensional arrangements of point sources, including axially aligned atoms, are successfully refocused on the screen, demonstrating the simultaneous and time-efficient detection of the three-dimensional holographic imaging. We expect that non-sequential real-time measurements of three-dimensional point sources shall be in particular useful for quantum correlation measurements and *in situ* tracking of dynamic particles.

1. Introduction

In recent years, optical engineering of quantum systems has witnessed very rapid technological progress. One good example is optical trapping of single atoms in synthetic structures of a few micrometers in size [1–3]. In conjunction with Rydberg-atom interactions, these optically-driven quantum systems are referred to as Rydberg-atom quantum simulators and demonstrated 20-qubit GHZ state generation [4], 50-qubit quantum annealing [5], and quantum simulations of Ising-type [6,7] or XY spin models across phase transitions [8]. Currently, being fueled by the desire to reach the quantum advantage regime [9], improvements of these systems are being actively investigated in their performance and scale. As far as optical technologies are concerned, improvements can be made in areas of trapping, manipulating, and probing. For the first two, making optical traps as many as $N = 1000$ [10] and optical quantum gates of extreme precision [11] are being investigated. For the last, we consider in this paper an efficient, three-dimensional (3D) optical probing of quantum systems. Simultaneous detection of 3D atoms, which is 3D point-source imaging in optics, is expected to be of particular importance in 3D qubit applications [12–14] and also in other applications requiring non-sequential measurements [15].

Obtaining the volumetric information of a 3D distribution of point sources all at once is an interesting and challenging optical problem [16]. Conventional 3D imaging modalities like computational tomography [17], magnetic resonance imaging [18], or ultrasonography [19], require tomographic two-dimensional (2D) images, in order to reconstruct a 3D image, so such a multi-shot sequential method costs computational resources as well as processing time. Pin-hole camera imaging [20] or extended depth-of-field imaging [21] can map 3D objects on to a 2D screen all at once, but their axial information is lost. Fresnel incoherent correlation holography [22] allows acquiring interference-based 3D information, while it requires at least three camera shots and reconstruction process. If the axial positions are given as a priori information, direct

#415805 https://doi.org/10.1364/OE.415805
Journal © 2021 Received 11 Dec 2020; revised 14 Jan 2021; accepted 19 Jan 2021; published 25 Jan 2021

Optics EXPRESS

3D imaging that preserves complete 3D volumetric information may be possible. One example along this approach is the use of multi-focal grating [23], which implements N different focal lengths in one grating device so that as-many tomographic images are simultaneously projected on to N different sections of a large screen; nonetheless, this method produces unwanted N-1 ghost images [24] and thus demands extra exposure time. The extended imaging time is often less favorable in applications that can benefit from one-shot 3D imaging.

In this study, we demonstrate a method to use space-variant holographic functions [25] for one-shot 3D imaging. The central concept of our method originates from the optical conformal mapping, best known as “imaging on curved surfaces" [26], which uses a computer-generated hologram (CGH) to map an object plane on to a curved screen. In our method (3D holographic imaging, hereafter), the optical direction is reversed so that “3D scattered point sources" are mapped on to one image plane. One example is shown in Fig. 1, where twelve single atoms are used as individual point fluorescence sources and the 3D holographic imaging method, to be described in Sec. 2, can properly image the otherwise unimaged atoms. In the rest of the paper, we first describe the working principle of the proposed method in Sec. 2 and, after briefly explaining the experimental procedure in Sec. 3, we present a few exemplary demos along with their performance summary in Sec. 4. The conclusion follows in Sec. 5.

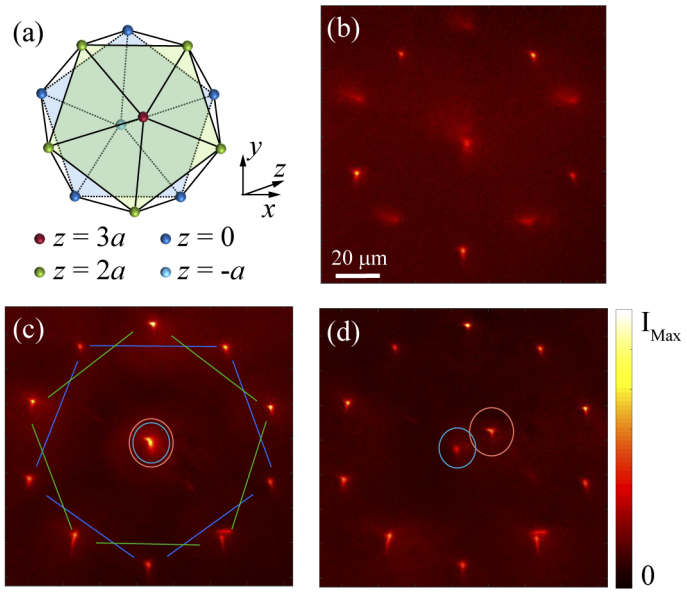

Fig. 1. (a) The icosahedron configuration of twelve (N = 12) single atoms on four different axial planes, respectively at $z = -a$, 0, $2a$, and $3a$ (a = 8 μm). (b) Conventional imaging with an insufficient depth of field (DOF, $z_{\mathrm{DOF}} = \lambda/\mathrm{NA}^2$ = 3.1 μm for NA = 0.5 and λ = 780 nm). (c,d) 3D holographic imaging (c) with axial displacements only and (d) with both axial and lateral displacements.

2. Holographic 3D imaging

The key idea of 3D holographic imaging is wave-front shaping on a quasi-image plane (QIP). The images of point sources are blurred on QIP and their spatial frequency components are strongly coupled with QIP coordinates. So, wave-front shaping on QIP can individually redirect and thus focus the point spreads of the point sources. A schematic setup is shown in Fig. 2, which consists

Optics EXPRESS

of a two-lens microscope, a relay lens to the screen, and a spatial light modulator (SLM) placed on the QIP.

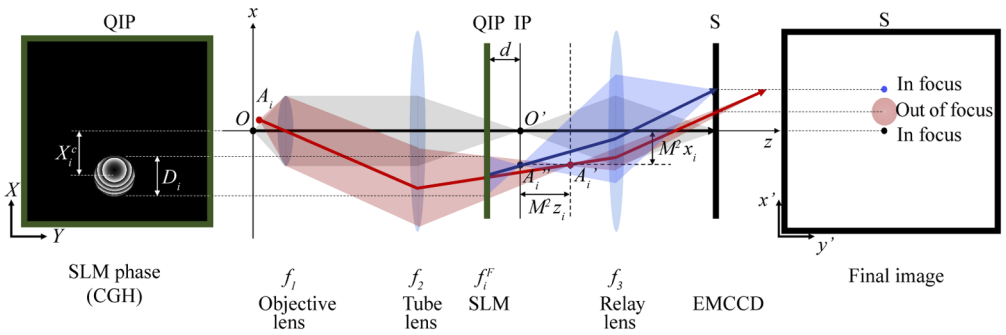

Fig. 2. Optical layout of the 3D holographic imaging microscope, which consists of an objective lens (of focal length f_1), a tube lens (f_2), an SLM at the quasi-image plane (QIP), and a relay lens (f_3) to the final image screen (S). The red line indicates the chief ray of a point source $A_i = (x_i, y_i, z_i)$ to the original, unshaped image $A_i' = (-Mx_i, -My_i, 2L + M^2 z_i)$ on the intermediate image plane (IP), which results in an out-of-focus screen image. With a Fresnel lenslet programmed on the QIP, which is separated by d from the IP, the redirected ray (blue line) is focused on to IP. The left-hand side figure shows the CGH pattern $\Phi_{\text{SLM}}(X, Y)$ of the Fresnel lenslet and the right-hand side figure compares the original and as-focused images on the screen.

In this setup, point source $A_i(x_i, y_i, z_i)$ is otherwise (without wave-front shaping) imaged at $A_i'(-Mx_i, -My_i, 2L + M^2 z_i)$, where $M = f_2/f_1$ is the magnification and $L = f_1 + f_2$. The axial and lateral shifts are given by $(x_i', y_i') = (-Mx_i, -My_i)$ and $z_i' = M^2 z_i$, respectively, from the image O' of the origin. So, the space-variant phase function of the point spread on the QIP is given by

$$\phi_i(X, Y) = \frac{k}{2(d + z_i')} \left((X - x_i')^2 + (Y - y_i')^2 \right), \tag{1}$$

where X, Y denote the QIP lateral coordinates, $k = 2\pi/\lambda$ is the wave number, and d is the separation between the QIP and the image plane (IP). The wave-front shaping in our 3D holographic imaging intends to direct the focus at A_i' to $A_I'' = (x_i', y_i', 2L)$ on the image plane. For that, the phase $\phi_i(X, Y)$ is eliminated and a quadratic phase function (Fresnel lens) is programmed to focus the remaining planar beam. So, the resulting phase function is given by

$$\Phi_i(X, Y) = \frac{k}{2f_i^{\text{F}}} \left((X - x_i')^2 + (Y - y_i')^2 \right) \tag{2}$$

with $f_i^{\text{F}} = d(d + z_i')/z_i'$ the focal length of the Fresnel lenslet to be programmed.

For N point sources, the phase functions Φ_i (for $i = 1, \ldots, N$) are to be superposed, which is permitted as long as the intensity profiles of the beams on the QIP are non-overlapping with each other. (If the profiles are in part overlapping, the phase functions are to be sectioned appropriately.) According to *ABCD* matrix calculation, the ray center, (X_i^c, Y_i^c), and the light-cone diameter, D_i, of the i^{th} QIP beam are respectively given by

$$(X_i^c, Y_i^c) = \left(1 + \frac{d + z_i'}{M^2 f_1 - z_i'} \right) (x_i', y_i') \tag{3}$$

$$D_i = \frac{2\text{NA}}{M} |d + z_i'|, \tag{4}$$

Optics EXPRESS

where NA is the numerical aperture of the entrance pupil. The total phase function of the required N Fresnel lenslets is then given by

$$\Phi(X,Y) = \sum_{i=1}^{N} \Phi_i(X,Y)\, H\left((X-X_i^c)^2 + (Y-Y_i^c)^2 - \frac{D_i^2}{4}\right), \tag{5}$$

where $H(x)$ is the Heaviside step function defined by $H(x) = 1$ (0) for $x>0$ ($x<0$).

3. Experimental procedure

As an experimental demonstration of the 3D holographic imaging, we use isolated single atoms as point sources. The atoms are positioned in three-dimensional free space with optical tweezers (far-off resonant optical dipole traps). The details of the atom arrangements are reported elsewhere [3,14,27]. In brief, the atoms (rubidium, ^{87}Rb) are first cooled below 100 μK in a 10^{-10} Torr vacuum chamber by Doppler and polarization-gradient cooling, and optically pumped to the ground hyper-fine state $|5S_{1/2}, F = 2\rangle$. Then, optical tweezers are produced through Fourier-domain phase modulation by an SLM (the trapping SLM, Meadowlark 512×512). The optical tweezers are frequency-centered at 808 nm and the beam radius is $w_0 = 1$ μm, reduced by 1/25 in a two-lens relay system. For defect-free arrangements of atoms [14], the trapping SLM is programmed to rearrange the optical tweezers and the atoms are monitored with an electron-multiplying charge-coupled device (EMCCD) camera which detects the fluorescence of the optical cycling transition (of $\lambda = 780$ nm) to $|5P_{3/2}, F' = 3\rangle$.

For our 3D holographic imaging, an auxiliary apparatus is incorporated in the above cold-atom system. The apparatus consists of an additional two-lens ×50 magnifier (of $f_1 = 4$ mm, NA=0.5 and $f_2 = 200$ mm), another SLM (the imaging SLM, Meadowlark 1920×1152), and a single-lens relay (of $f_3 = 100$ mm) to the EMCCD. The phase-modulated light by the imaging SLM is filtered out with a 780-nm half-wave plate and a polarizer (parallel to the SLM's slow axis). The imaging SLM is placed on the QIP at $d = 60$ mm apart from the two-lens magnifier's image plane (IP) and computer-programmed the Fresnel lenslets with Eq. (5). The images on the IP are relayed to the screen, where the EMCCD records the focused atom fluorescence. Resulting images are verified with a tomographic imaging using an electrically tunable lens (ETL) [12].

4. Results and discussions

With the setup described above, we first test the working principle of the 3D holographic imaging. As shown in Fig. 3(a), we locate three atoms, A1-A3, on two different object planes, P1 and P2, separated by about five times the DOF ($z_{\mathrm{DOF}} = 3.1$ μm) so that conventional imaging does not properly image the three atoms all at once. For the 3D holographic imaging, we program a Fresnel lenslet (of focal length $f_{\mathrm{F}} = 150$ mm) only for A3 and no phases for A1 and A2. In addition, for a null test, we program the same Fresnel lenslet in the no-atom region (A0). The phase function $\Phi(X,Y)$ is programmed with Eq. (5), as shown in Fig. 3(b). In this case, the depth of field of the optical system is about five times smaller than the separation, $\Delta z = 16$ μm, between the image planes; therefore, as observed in Fig. 3(c), A1 and A3 are properly imaged but A2 is not. The peak intensities are plotted in Fig. 3(d) indicating that the holographic image of A3 is over 80% of the A1 image, mostly due to the diffraction efficienty of 84%. In comparison, the intensities of the no-image of $A3$ and the null test of $A0$ are less than 12%.

It is noted that there are certain axial regions which do not allow Fresnel-lens programming and that the atoms in the above experiment are chosen in allowed regions. There are two available object regions given by

$$\text{Region 1:} z_{\min} < z < z_{\mathrm{blind}} - z_{\mathrm{DOF}} \tag{6}$$

$$\text{Region 2:} z_{\mathrm{blind}} + z_{\mathrm{DOF}} < z < z_{\max} \tag{7}$$

Optics EXPRESS

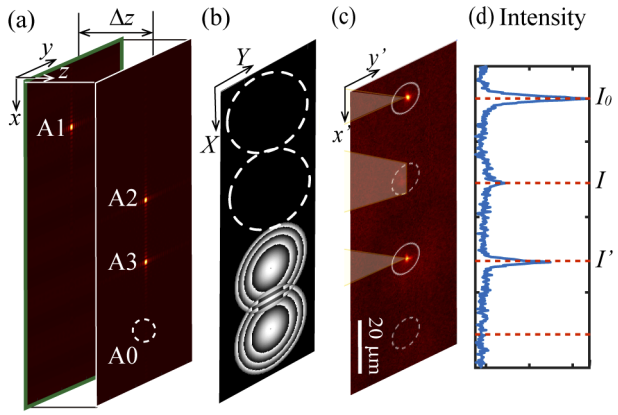

Fig. 3. (a) Three atoms (A1, A2, and A3) on two different object planes ($z = 0$ and $z = 5.2\ z_{\mathrm{DOF}}$). (b) The phase pattern $\Phi_{\mathrm{SLM}}(X, Y)$ programmed to refocus A3 and a null point source (A0). (c) Resulting images of the 3D holographic imaging. (d) Light intensity profiles of the images, compared with the null image.

where z_{min} and z_{max} are the upper and lower bounds given by Nyquist theorem. As the phase difference between adjacent SLM pixels cannot exceed π, the programmable Fresnel focal length is lower bounded by the Nyquist focal length [28], i.e., $f_{\mathrm{F}}(z) = |d(d + M^2 z)/M^2 z| > f_{\mathrm{Nyquist}} = \Delta D/\lambda$, where $D = 2\mathrm{NA}|d + z_i'|/M$ is the diameter of the phase patch (or the QIP beam size) and Δ is the pixel size of the SLM. So, the resulting z_{min} and z_{max} are given by $z_{\mathrm{max}} = -z_{\mathrm{min}} = d\lambda/2M\Delta\mathrm{NA}$. Also, $z_{\mathrm{blind}} = -d/M^2$ is the blind spot, in which an object is sharply focused on to the QIP. In this case, the phase patch size is given too small to program a Fresnel lens. As the axial width of the focal volume is the Abbe DOF, the blind region is given by $z_{\mathrm{blind}} - z_{\mathrm{DOF}} < z < z_{\mathrm{blind}} + z_{\mathrm{DOF}}$. In our experimental setup of NA = 0.5, $\Delta = 9.2\ \mu$m, $d = 60$ mm, $M = 50$, and $\lambda = 780$ nm, the available axial regions are given by $-100\ \mu\mathrm{m} < z < -27\ \mu\mathrm{m}$ and $-21\ \mu\mathrm{m} < z < 100\ \mu\mathrm{m}$.

Now we image atoms on a curved surface using the 3D holographic imaging method. Nine atoms are arranged on a hyperbolic paraboloid defined by $z/z_0 = 1 + (x/x_0)^2 - (y/y_0)^2$ with $x_0 = 1.1 \times 10^{-9}\ \mu$m, $y_0 = 7.7 \times 10^{-10}\ \mu$m, and $z_0 = 8.0\ \mu$m. As in Fig. 4(a), we use five different axial planes of respective axial positions $z = (-46, 0, 8, 16, 32)\ \mu$m, where the first plane belongs to Region 1 and the rest in Region 2. The CGH of Fresnel lenslets for the atoms on the $z \neq 0$ planes is programmed with Eq. (5) and is shown in Fig. 4(b). Note that the phase and intensity centers, given in Eqs. (3) and (4), do not coincide as their axial positions differ. The resulting images, without and with the CGH, are shown in Figs. 4(c) and 4(d), respectively. While the former exhibits only the two atoms on the $z = 0$ plane, the latter shows all atoms distinctively. In Fig. 4(e), the distribution of the peak intensities (I/I_0) vs the widths (w/w_0) of the unshaped images (blue) and the 3D holographic images (red), respectively from Fig. 4(c) and 4(d), where I_0 and w_0 are $z = 0$-plane values. The statistics shows that the 3D holographic imaging improves the intensities from $\langle I/I_0 \rangle = 0.27 \pm 0.43$ to 1.10 ± 0.34 (410% improvement) and the beam widths from $\langle w/w_0 \rangle = 3.64 \pm 2.10$ to 1.27 ± 0.34 (290% improvement).

The 3D holographic imaging can not only axially but also laterally relocate images. We use axially aligned atoms, as in Fig. 5(a), and use the 3D holographic imaging method to separate their otherwise overlapping images. We trap three atoms respectively at $z = -a, 0, a$ with $a = 13\ z_{\mathrm{DOF}} = 40\ \mu$m in such a way that atom A1 is located in Region 1 of Eq. (6) and atoms A2 and A3 in Region 2. First, the CGH, $\Phi^a_{\mathrm{SLM}}(X, Y)$, is programmed with Eq. (1) for axial shifts only, which is shown in Fig. 5(b): two Fresnel lensets for A1 (green) and A3 (blue) are programmed, along with the null phase for A3 (yellow), in such a way that A2 and A3 lenslets

Optics EXPRESS

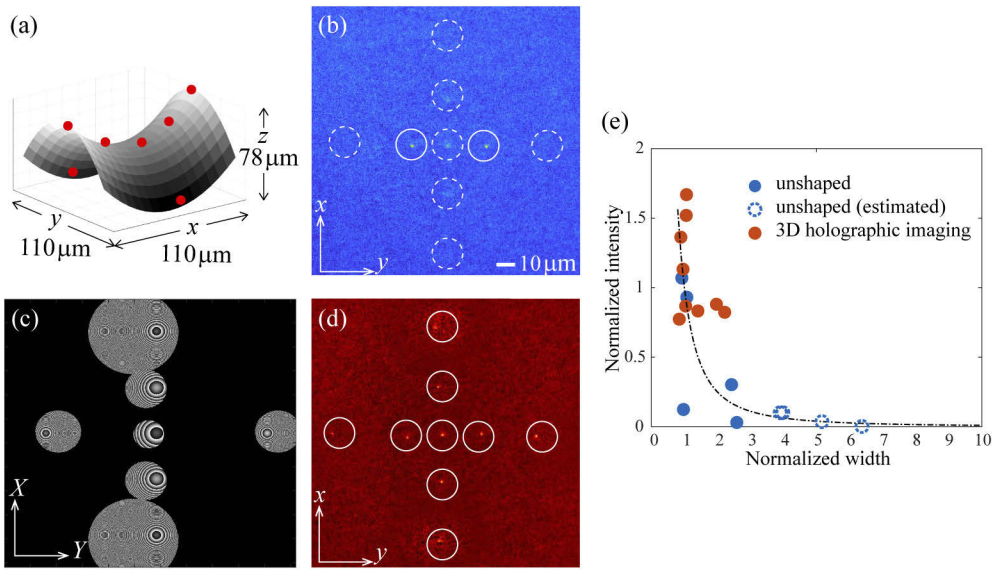

Fig. 4. (a) Nine atoms are placed on the surface of a hyperbolic paraboloid (a saddle-shape), on five different axial layers, respectively, at $z/z_{\mathrm{DOF}} = -15.3, 0.0, 2.6, 5.3$, and 10.2. (b) Conventional images of the atoms without the Fresnel lenslet programming. (c) The CGH $\Phi_{\mathrm{SLM}}(X, Y)$ of Fresnel lenslets for the seven atoms on the $z \neq 0$ planes. (d) The resulting 3D holographic image. (e) The peak intensities and widths of conventional (blue) and 3D holographic (red) images (normalized with the $z = 0$ plane values).

are superposed while A1 is sectioned. Note that the Fresnel lensets (circled intensity functions) in Fig. 5(b) are not concentric ($Y_1^c \neq Y_2^c \neq Y_3^c$) as $y_i \neq 0$ ($y_0 = 880\ \mu$m), while the phase functions are concentric as the atoms are axially aligned ($x_1 = x_2 = x_3 = 0$ and $y_1 = y_2 = y_3 = y_0$). As expected the resulting images, shown in Fig. 5(c), overlap with each other at the QIP image center $(X, Y) = (0, 0)$. Now in order to separate the overlapping images, we use additional linear-phase functions, i.e.,

$$\Phi_{\mathrm{SLM}}^{a,l}(X, Y) = \Phi_{\mathrm{SLM}}^{a}(X, Y) + k_{\mathrm{Li}} Y. \tag{8}$$

As an example, the phase and intensity centers of the QIP beams can be matched as in Fig. 5(d) with $k_{\mathrm{Li}} = 9kM^2 w_0/a = 6.4 \times 10^4\ m^{-1}$ so that the separation of the final images is about nine times the spot size of the final images ($M^2 w_0 = 50\ \mu$m). The resulting images are well separated as shown in Fig. 5(e) with 100%, 46%, and 85% peak intensities compared to non-overlapping ones, respectively.

We now discuss the maximal volume and the maximal atom number allowed for the 3D imaging scheme. First, the max volume $V_{\mathrm{max}} = L_x L_y L_z$ can be estimated using *ABCD* matrix calculation, where the lateral extents L_x and L_y are given by

$$L_{x,y} = \frac{L_{x,y}^{\mathrm{SLM}}}{M} \frac{f_2 + Dd/L_{x,y}^{\mathrm{SLM}}}{f_2 + d/M} \tag{9}$$

and the axial extent $L_z = 2z_{\mathrm{max}} - 2z_{\mathrm{DOF}}$ is the sum of two regions defined in Eqs. (6) and (7). In the current setup, $L_x^{\mathrm{SLM}} = 17.6$ mm and $L_y^{\mathrm{SLM}} = 10.7$ mm, so we get $V_{\mathrm{max}} = 326 \times 189 \times 194\ \mu\mathrm{m}^3$. Second, the max number N_{max} of point sources allowed for the 3D holographic imaging is strongly dependent on their distribution nature. When we use, as the criteria of successful imaging, the peak intensity condition, $I > 0.6 I_0$, where I is the 3D holographic imaging intensity and I_0 is the convnetional imaging intensity at the $z = 0$ plane, we get $N_{\mathrm{max}} > 200$, e.g., in an

Optics EXPRESS

AB-stacked $10 \times 10 \times 2$ square array with a lattice constant of $a = 40$ μm. As for a random distribution of atoms, our Monte Carlo simulation estimates that about 65 (84) atoms can be successfully imaged out of 100 (200) atoms randomly sampled from $V_{\max}$. These numbers of $N_{\max}$ can be greatly increased at the price of single-shot imaging, for example, by using ETL [12]. In addition, ETL shall be in particular useful to remove the blind zone defined in Eqs. (6) and (7). Hardware improvements can be considered to increase $N_{\max}$: as $V_{\max} \approx L_{SLM}/M\Delta$, three times larger L_{SLM} and two times smaller Δ could achieve $N = 10^3$ on the scale of next-generation quantum computers [10].

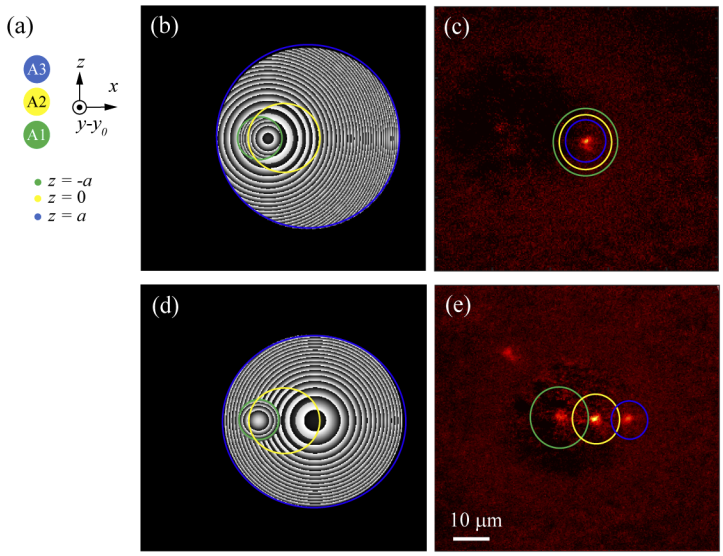

Fig. 5. (a) Axially aligned three atoms (of respective positions $z = -a, 0$, and a with $a = 13\ z_{\mathrm{DOF}}$). (b) The CGH $\Phi^{a}_{\mathrm{SLM}}(X, Y)$ for axial shifts only, in which green, yellow, and blue circles are for A1, A2, and A3, respectively. (c) The resulting image with Φ^{a}_{SLM}. (d) The CGH $\Phi^{a,l}_{\mathrm{SLM}}$ for both axial and lateral rearrangements. (e) The resulting image of the 3D holographic imaging, in which the upper-left spot is the 0^{th} order diffraction of the trapping SLM.

5. Conclusions

In summary, we have demonstrated 3D holographic imaging for volumetric fluorescence detection. The wave-front of 3D point sources is programmed with local-conformal mapping to achieve simultaneous and time-efficient planar imaging. For that, Fresnel lenslets are programmed with an SLM to render 3D holographic imaging of an atom array all at once. It is estimated that over $N_{\max} = 200$ atoms in a volume of $V_{\max} = 1.2 \times 10^7$ μm^3 can be simultaneously imaged with our method. With currently available fabrication technologies [29], the possible number of imaging points could be scaled to $N = 10^3$ [10]. It is hoped that the method shall be useful for non-sequential real-time measurements of 3D point sources in applications of quantum correlation measurements [30] or *in situ* tracking of dynamic particles [31,32].

Funding. Samsung Science and Technology Foundation (SSTF-BA1301-12); National Research Foundation of Korea (2017R1E1A1A01074307); Air Force Office of Scientific Research (FA2386-20-1-4068).

Acknowledgements. The authors thank Guido Burkard for fruitful discussion.

Disclosures. The authors declare no conflicts of interest.

Optics EXPRESS

References

1. M. Endres, H. Bernien, A. Keesling, H. Levine, E. R. Anschuetz, A. Krajebrink, C. Senko, V. Vuletić, M. Greiner, and M. D. Lukin, "Atom-by-atom assembly of defect-free one-dimensional cold atom arrays," Science **354**(6315), 1024–1027 (2016).
2. D. Barredo, S. de Léséleuc, V. Lienhard, T. Lahaye, and A. Browaeys, "An atom-by-atom assembler of defect-free arbitrary two-dimensional atomic arrays," Science **354**(6315), 1021–1023 (2016).
3. H. Kim, W. Lee, H. Lee, H. Jo, Y. Song, and J. Ahn, "In situ single-atom array synthesis using dynamic holographic optical tweezers," Nat. Commun. **7**(1), 13317 (2016).
4. A. Omran, H. Levine, A. Keesling, G. Semeghini, T. T. Wang, S. Ebadi, H. Bernien, A. S. Zibrov, H. Pichler, S. Choi, J. Cui, M. Rossignolo, P. Rembold, S. Montangero, T. Calarco, M. Endres, M. Greiner, V. Vuletić, and M. D. Lukin, "Generation and manipulation of Schrödinger cat states in Rydberg atom arrays," Science **365**(6453), 570–574 (2019).
5. H. Bernien, S. Schwartz, A. Keesling, H. Levine, A. Omran, H. Pichler, S. Choi, A. S. Zibrov, M. Endres, M. Greiner, V. Vuletić, and M. D. Lukin, "Probing many-body dynamics on a 51-atom quantum simulator," Nature **551**(7682), 579–584 (2017).
6. H. Kim, Y. J. Park, K. Kim, H.-S. Sim, and J. Ahn, "Detailed balance of thermalization dynamics in Rydberg-atom quantum simulators," Phys. Rev. Lett. **120**(18), 180502 (2018).
7. A. Keesling, A. Omran, H. Levine, H. Bernien, H. Pichler, S. Choi, R. Samajdar, S. Schwartz, P. Silvi, S. Sachdev, P. Zoller, M. Endres, M. Greiner, V. Vuletić, and M. D. Lukin, "Quantum Kibble-Zurek mechanism and critical dynamics on a programmable Rydberg simulator," Nature **568**(7751), 207–211 (2019).
8. V. Lienhard, S. de Léséleuc, D. Barredo, T. Lahaye, A. Browaeys, M. Schuler, L. P. Henry, and A. M. Läuchli, "Observing the space- and time-dependent growth of correlations in dynamically tuned synthetic Ising models with antiferromagnetic interactions," Phys. Rev. X **8**(2), 021070 (2018).
9. F. Arute, K. Arya, R. Babbush, D. Bacon, J. C. Bardin, R. Barends, R. Biswas, S. Boixo, F. G. S. L. Brandao, D. A. Buell, B. Burkett, Y. Chen, Z. Chen, B. Chiaro, R. Collins, W. Courtney, A. Dunsworth, E. Farhi, B. Foxen, A. Fowler, C. Gidney, M. Giustina, R. Graff, K. Guerin, S. Habegger, M. P. Harrigan, M. J. Hartmann, A. Ho, M. Hoffmann, T. Huang, T. S. Humble, S. V. Isakov, E. Jeffrey, Z. Jiang, D. Kafri, K. Kechedzhi, J. Kelly, P. V. Klimov, S. Knysh, A. Korotkov, F. Kostritsa, D. Landhuis, M. Lindmark, E. Lucero, D. Lyakh, S. Mandrá, J. R. McClean, M. McEwen, A. Megrant, X. Mi, K. Michielsen, M. Mohseni, J. Mutus, O. Naaman, M. Neeley, C. Neill, M. Y. Niu, E. Ostby, A. Petukhov, J. C. Platt, C. Quintana, E. G. Rieffel, P. Roushan, N. C. Rubin, D. Sank, K. J. Satzinger, V. Smelyanskiy, K. J. Sung, M. D. Trevithick, A. Vainsencher, B. Villalonga, T. White, Z. J. Yao, P. Yeh, A. Zalcman, H. Neven, and J. M. Martinis, "Quantum supremacy using a programmable superconducting processor," Nature **574**(7779), 505–510 (2019).
10. A. Morello, "What would you do with 1000 qubits?" Quantum Sci. Technol. **3**(3), 030201 (2018).
11. I. S. Madjarov, J. P. Covey, A. L. Shaw, J. Choi, A. Kale, A. Cooper, H. Pichler, V. Schkolnik, J. R. Williams, and M. Endres, "High-fidelity entanglement and detection of alkaline-earth Rydberg atoms," Nat. Phys. **16**(8), 857–861 (2020).
12. D. Barredo, V. Lienhard, S. de Léséleuc, T. Lahaye, and A. Browaeys, "Synthetic three-dimensional atomic structures assembled atom by atom," Nature **561**(7721), 79–82 (2018).
13. Y. Song, M. Kim, H. Hwang, W. Lee, and J. Ahn, "Quantum annealing of Cayley-tree Ising spins," arxiv:2011.01653.
14. M. Kim, Y. Song, J. Kim, and J. Ahn, "Quantum-Ising Hamiltonian programming in trio, quartet, and sextet qubit systems," PRX Quantum **1**(2), 020323 (2020).
15. H. F. Hofmann, "Sequential measurements of non-commuting observables with quantum controlled interactions," New J. Phy. **16**(6), 063056 (2014).
16. J. Mertz, "Strategies for volumetric imaging with a fluorescence microscope," Optica **6**(10), 1261–1268 (2019).
17. D. T. Ginat and R. Gupta, "Advances in computed tomography imaging technology," Annu. Rev. Biomed. Eng. **16**(1), 431–453 (2014).
18. P. Irrazabal and D. G Nishmura, "Fast three dimensional magnetic resonance imaging," Magn. Reson. Med. **33**(5), 656–662 (1995).
19. M. J. Gooding, S. Kennedy, and J. A. Noble, "Volume reconstruction from sparse 3D ultrasonography," In: R. E. Ellis and T. M. Peters, eds., *Medical Image Computing and Computer-Assisted Intervention*, Lecture Notes in Computer Science 2879 (Springer, Berlin, 2003).
20. R. E. Swing and D. P. Rooney, "General transfer function for the pinhole camera," J. Opt. Soc. Am. **58**(5), 629–635 (1968).
21. S. Banerji, M. Meem, A. Majumder, B. Sensale-Rodriguez, and R. Menon, "Extreme-depth-of-focus imaging with a flat lens," Optica **7**(3), 214–217 (2020).
22. J. Rosen and G. Brooker, "Non-scanning motionless fluorescence three-dimensional holographic microscopy," Nat. Photonics **2**(3), 190–195 (2008).
23. S. Abrahamsson, J. Chen, B. Hajj, S. Stallinga, A. Y. Katsov, J. Wisniewski, G. Mizuguchi, P. Soule, F. Mueller, C. D. Darzacq, X. Darzacq, C. Wu, C. I. Bargmann, D. A. Agard, M. Dahan, and M. G. L. Gustafsson, "Fast multicolor 3D imaging using aberration-corrected multifocus microscopy," Nat. Methods **10**(1), 60–63 (2013).
24. C. Maurer, S. Khan, S. Fassl, S. Bernet, and M. Ritsch-Marte, "Depth of field multiplexing in microscopy," Opt. Express **18**(3), 3023–3034 (2010).

Optics EXPRESS

25. T. F. Krile, R. J. Marks, J. F. Walkup, and M. O. Hagler, "Holographic representations of space-variant systems using phase-coded reference beams," Appl. Opt. **16**(12), 3131–3135 (1977).
26. W. H. Lee and O. Bryngdahl, "Imaging on curved surfaces," Opt. Commun. **12**(4), 382–385 (1974).
27. W. Lee, H. Kim, and J. Ahn, "Three-dimensional rearrangement of single atoms using actively controlled optical microtraps," Opt. Express **24**(9), 9816–9825 (2016).
28. D. M. Cotrell and R. A. Lily, "Multiple imaging phase-encoded optical elements written as programmable spatial light modulators," Appl. Opt. **29**(17), 2505–2509 (1990).
29. Y.-H. Kim, S. M. Cho, K. Choi, C. Y. Hwang, G. H. Kim, S. Cheon, and C.-S. Hwang, "Crafting a 1.5 μm pixel pitch spatial light modulator using $Ge_2Sb_2Te_5$ phase change material," J. Opt. Soc. Am. A **36**(12), D23–D30 (2019).
30. M. E. Shea, P. M. Baker, J. A. Joseph, J. Kim, and D. J. Gauthier, "Sub-ms, nondestructive, time-resolved quantum-state readout of a single, trapped neutral atom," Phys. Rev. A **102**(5), 053101 (2020).
31. H. Qian, "Single-particle tracking: Brownian dynamics of viscoelastic materials," Biophys. J. **79**(1), 137–143 (2000).
32. M. Dahan, S. Levi, C. Luccardini, P. Rostaing, B. Riveau, and A. Triller, "Diffusion dynamics of glycine receptors revealed by single-quantum dot tracking," Science **302**(5644), 442–445 (2003).